Wiley Analytical Science

The Current State of Reconstruction Technologies for 3D X-ray Microscopy including Algorithmic Innovation for AI-based Recovery

April 26, 10:00am - 11:00am EDT

Many properties can only be fully understood in 3D, such as porosity and tortuosity in porous materials, network connection maps in neuroscience, or mechanical properties in 3D additively manufactured structures. X-ray microscopy provides a unique method to image samples non-destructively in 3D across a wide range of materials and life sciences.

Watch this session during the WAS Virtual Conference:

Nicolas Guenichault, Ph.D.

Dr. Stephen T. Kelly, Ph.D.

Register Now

This talk is sponsored by ZEISS

ADVANCED OPTICAL MATERIALS
www.advopticalmat.de

High-Quality $CsPbBr_3$ Perovskite Films with Modal Gain above 10 000 cm^{-1} at Room Temperature

Dmitry A. Tatarinov, Sergey S. Anoshkin, Ivan A. Tsibizov, Volodymyr Sheremet, Furkan Isik, Alexey Y. Zhizhchenko, Artem B. Cherepakhin, Aleksandr A. Kuchmizhak, Anatoly P. Pushkarev, Hilmi Volkan Demir,* and Sergey V. Makarov**

Halide perovskite lasers based on $CsPbBr_3$ micro- and nanoscale crystals have demonstrated fascinating performance owing to their low-threshold lasing at room temperature and cost-effective fabrication. However, chemically synthesized thin films of $CsPbBr_3$ usually have rough polycrystalline morphology along with a large amount of crystal lattice defects and, thus, are mostly utilized for the engineering of light-emitting devices. This obstacle prevents their usage in many photonic applications. Here, a protocol to deposit large-grain and smooth $CsPbBr_3$ thin films is developed. Their high quality and large scale allow to demonstrate a maximum optical gain up to 12 900 cm^{-1} in the spectral range of 530–540 nm, which is a record-high value among all previously reported halide perovskites and bulk semiconductors (e.g., GaAs, GaN, etc.) at room temperature. Moreover, femtosecond laser ablation technique is employed to create high-quality microdisc lasers on glass from these films to obtain excellent lasing characteristics. The revealed critical roles of thickness and grain size for the $CsPbBr_3$ films with extremely high optical gain pave the way for development of low-threshold lasers or ultimately small nanolasers, as well as to apply them for polaritonic logical elements and integrated photonic chips.

1. Introduction

Cesium lead halide perovskites ($CsPbX_3$; X = I, Br, Cl) represent a promising class of semiconductors for advanced micro- and nanolasers generating laser emission in the range of 420–824 nm,[1–4], which can be simply synthesized from solution. First of all, such perovskites possess relatively high refractive index (larger than 2), which allows for the creation of self-resonating gain media placed on various substrates: dielectrics,[1–4] metals,[5] nanostructured,[6] photonic crystals,[7] as well as integrated with waveguiding systems.[8–10] Also, chemically synthesized $CsPbX_3$ perovskite single crystals[11] of high quality and different shapes (cuboids,[12,13] wires, [1,14,15] plates[16–18]) exhibit high levels of optical gain (typically $\approx 10^3$ cm^{-1})[19] larger than those of thin polycrystalline films synthesized from solution (typically $\approx 10^2$ cm^{-1}). Thus, they provide a powerful technological tool for micro- and nanolasers fabrication, when their precise positioning is not required. However, the fabrication of large-scale films with crystalline quality as high as for single crystals would allow for overcoming many technological obstacles hindering lithographical creation[9,20,21] of highly controllable designs for lasing applications.

In this paper, we develop a high-temperature recrystallization method for chemical synthesis of large-grain $CsPbBr_3$ thin

D. A. Tatarinov, S. S. Anoshkin, I. A. Tsibizov, A. P. Pushkarev, S. V. Makarov
School of Physics and Engineering
ITMO University
197101 St. Petersburg, Russia
E-mail: anatoly.pushkarev@metalab.ifmo.ru; s.makarov@metalab.ifmo.ru

V. Sheremet, F. Isik, H. V. Demir
UNAM-Institute of Materials Science and Nanotechnology
Department of Electrical and Electronics Engineering
Department of Physics
Bilkent University
06800 Ankara, Turkey
E-mail: volkan@fen.bilkent.edu.tr

The ORCID identification number(s) for the author(s) of this article can be found under https://doi.org/10.1002/adom.202202407.

DOI: 10.1002/adom.202202407

A. Y. Zhizhchenko, A. A. Kuchmizhak
School of Engineering
Far Eastern Federal University
690091 Vladivostok, Russia

A. Y. Zhizhchenko, A. B. Cherepakhin, A. A. Kuchmizhak
Institute of Automation and Control Processes (IACP)
Far Eastern Branch of the Russian Academy of Science
690091 Vladivostok, Russia

H. V. Demir
LUMINOUS! Center of Excellence for Semiconductor Lighting and Displays
School of Electrical and Electronic Engineering
School of Physical and Materials Sciences
School of Materials Science and Engineering
Nanyang Technological University
Singapore 639798

S. V. Makarov
Qingdao Innovation and Development Center
Harbin Engineering University
Qingdao, Shandong 266000, China

films exhibiting giant optical gain. Namely, our variable stripe length (VSL) measurements reveal the exceeding of 10^4 cm^{-1} level for the modal gain in the most optimal thicknesses and quality of the film. The reported values of the maximum gain value are the record high among all halide perovskite materials surpassing previous records for perovskites by around two folds (5077 cm^{-1} for $CsPbBr_3$ single crystal microplatelets[19]). Moreover, the observed values of maximum modal gain and differential gain are one of the highest among all values reported for bulk semiconductors at room temperature.

To demonstrate the applicability of the high-gain films for controllable creation of microlasers, we employ direct femtosecond (fs) laser printing of perovskite whispering gallery mode microcavities, which was previously applied for polycrystalline films[22,23] and microcrystals.[24,25]

2. Results and Discussion

2.1. Thin Films Synthesis and Characterization

To fabricate large-grain (LG) $CsPbBr_3$ thin films we developed a new approach—high-temperature pressure-assisted recrystallization. First, small-grain (SG) polycrystalline perovskite films were spin-casted on glass substrates using 0.3 M perovskite precursor solution and, thereafter, gradually annealed on a hot plate (for detail, see Experimental Section). These so-called source films consist of pressed small grains with a mean lateral size $d \approx 200$ nm and have numerous pin-holes and cracks (inset image in **Figure 1**d). Their average thickness is about $h \approx 70$ nm and their mean roughness is $R = 20$ nm (inset image in Figure 1e). Second, two samples were pressed down in a face-to-face manner using a U-shape metal bracket and a screw covered at its end with a cap nut as illustrated in Figure 1a, and, then, gradually annealed on a hot plate at high temperature (for details, see Experimental Section). The pressing down procedure gives an interference pattern around the point where the cap nut contacts the upper sample (Figure S1, Supporting Information). Such pressure-assisted annealing results in the formation of a thin LG perovskite film stuck to the surface of the upper substrate when the cooled-down samples are finally divided. In the area of ≈0.1 cm^2 close to the point at which the pressure is applied, we observed a uniform pinhole-free film in a bright-field optical image (Figure S2, Supporting Information). Examining this region upon 360 nm UV excitation revealed large crystalline domains emitting green light evenly distributed over their entire area. Stronger luminescence was observed at grain boundaries, which indicates in-plane light waveguiding inside the grains and its outcoupling via scattering (Figure 1b). A dark-field image of the same region demonstrates almost no scattering from the gain central parts revealing the grains boundaries (Figure 1c). Consequently, there are no submicron-sized crystallites within large perovskite grains. To emphasize a dramatic difference in crystallinity of the source films and recrystallized ones, fluorescent and dark-field optical images of the former are shown in the insets of Figures 1b and 1c, respectively.

Scanning electron microscopy (SEM) image visualized hairline cracks between the adjacent grains of a mean lateral size $d = 18.4$ μm (Figure 1d). Inspection of the surface morphology by atomic force microscopy (AFM) gave the roughness of the grains about $R_{mean} = 5$ nm. Interestingly, right at the grain boundaries the thickness ramps up. We assume a possible scenario for such ramp formation is the following:

i) annealing of the borosilicate glass substrates at 510 °C triggers their surface crystallization in the form of large domains; ii) the perovskite melts and fills trenches between the domains; and iii) dividing the substrates results in cracking the film at the trenches where the strain in perovskite film is maximum. Indeed, annealing of LG films occurs in the range between the glass transition temperature (496 °C) and the crystallization temperature (559 °C) of borosilicate glass[26] that could result in surface modification of the substrates. A solid evidence of the substrates surface crystallization is its fingerprints left on the perovskite film. Therefore, every single perovskite grain has its own quasi-periodic texture (Figure 1e). Along with this, a high resolution SEM image of the divided bottom substrate showed shallow trenches containing the traces of perovskite material removed from the film (Figure S3, Supporting Information).

To prove the excellent crystallinity of LG films, selected area electron diffraction (SAED) of a film fragment transferred to a TEM (transmission electron microscopy) grid was conducted. The SAED pattern measured along [010] zone axis reveals sharp diffraction spots assigned to (002), (200), (101), and (100) crystallographic planes of orthorhombic $CsPbBr_3$ (Figure 1f). X-ray diffraction (XRD) pattern of the film obtained in Bragg–Brentano geometry consists of two intense peaks at 15.2° and 30.7° 2θ corresponding to (110) and (220) parallel planes of orthorhombic cesium lead tribromide (space group P_{bnm}[27]), respectively (Figure 1g). The presence of these two peaks only in the pattern indicates superior out-of-plane crystallographic orientation of the perovskite grains. In contrast, their in-plane orientation is supposed to be random. Remarkably, XRD pattern of the small-grain film consists of multiple peaks that are broader than signals collected from the large-grain one (Figure 1g). Poor crystallinity, namely the small size of grains, and random spatial orientation of the latter are responsible for the established difference in the patterns. Additionally, the high crystallinity of the LG films was confirmed by Raman spectroscopy. The Raman spectrum collected from the single grains contains four peaks at 73, 127, 160, and 311 cm^{-1}, which match well with ones observed for single-crystal nanowires of the same chemical composition (see Supporting Information elsewhere[25]).

A comparison of basic optical properties between SG and LG films was made by measuring steady-state absorption and photoluminescence (PL) spectra. The absorption spectrum of the SG film shows exciton resonance peaked at wavelength $\lambda = 515$ nm and spectrally long tail assigned to Rayleigh scattering of the incident light by the rough surface of the film (Figure 1i). At the same time, LG film exhibits sharper cut-off because the improved surface morphology of the film does not cause any scattering (Figure 1i). The full width at half maximum ($\delta\lambda$) of the exciton peak for LG film ($\delta\lambda = 13.8$ nm) is smaller than that for SG one ($\delta\lambda = 19.4$ nm) (Figure S4, Supporting Information). A similar trend was observed for PL spectra of the samples: $\delta\lambda = 16.2$ and 17.5 nm for LG and SG films, respectively (Figure S4, Supporting Information). For the LG film, the

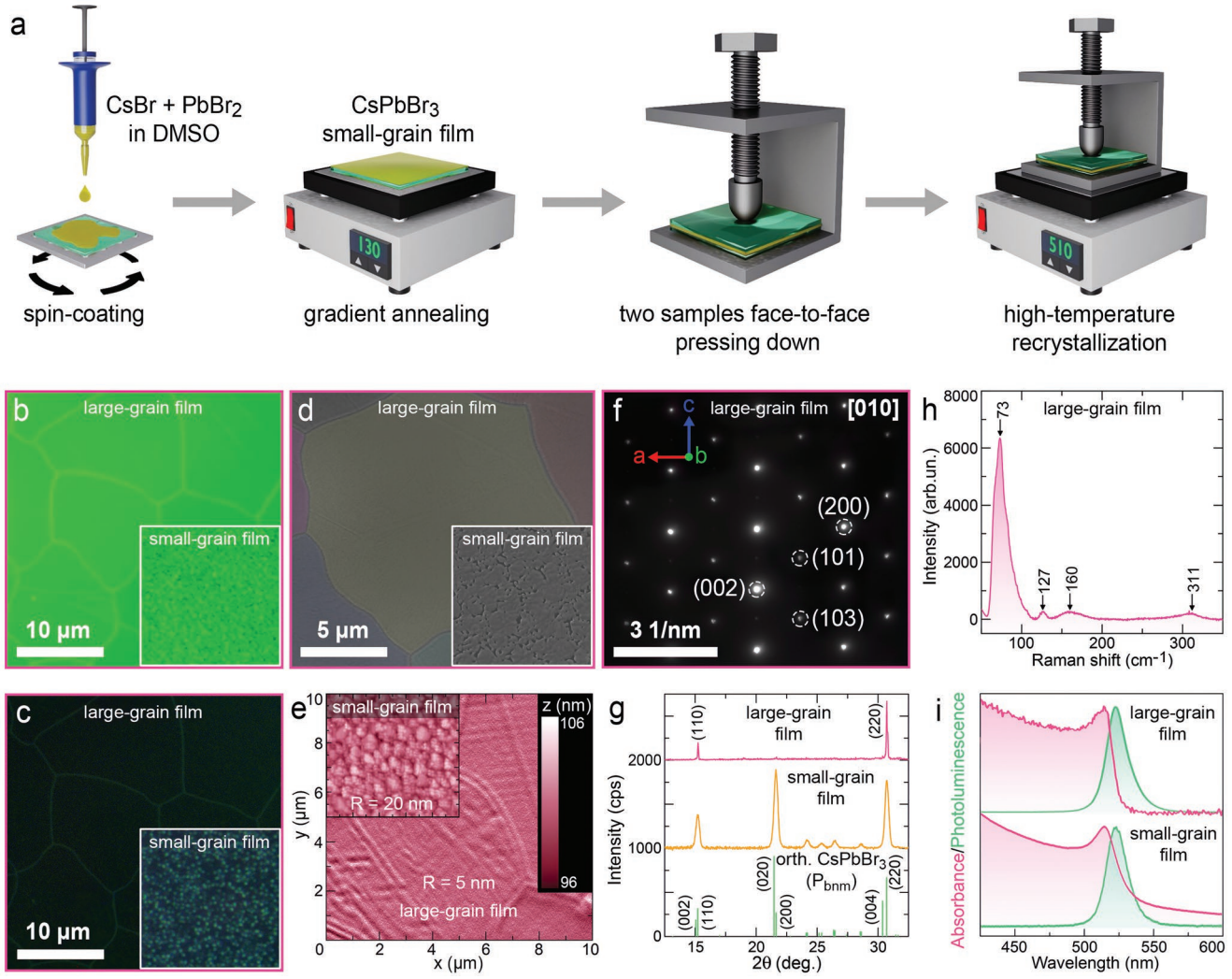

Figure 1. Large-grain $CsPbBr_3$ film fabrication, characterization, and comparison with a small-grain film. a) Schematic illustration of the approach employed for the preparation of perovskite large-grain (LG) films. b) Fluorescent image of the LG film exhibiting a remarkable outcoupling of emission at grain boundaries. Inset: fluorescent image of a small-grain (SG) film. c) Dark-field image of the LG film showing the absence of microcrystalline scattering centers within single grains. Inset: image confirming pronounced scattering of light by SG film. d) False color top-view SEM image of the LG film surface visualizing hairline cracks between its large grains. Inset: corresponding image of the SG film demonstrating co-crystallized tiny grains along with numerous pinholes and cracks. e) AFM image of the LG film surface. Every single grain reveals a unique quasi-periodic texture with roughness not exceeding 5 nm. Inset: image of the SG film exhibiting roughness of about 20 nm. f) SAED pattern of a small piece of the LG film measured along [010] zone axis. Crystal lattice orientation is additionally defined with orthorhombic (P_{bnm}) unit cell vectors (*a*, *b*, *c*). g) XRD patterns of SG and LG films collected in Bragg–Brentano geometry as well as reference data for orthorhombic $CsPbBr_3$ (P_{bnm}). Two peaks in the pattern of the LG film belong to parallel planes (110) and (220) and confirm out-of-plane crystallographic orientation of the film. The pattern of the SG film consists of many peaks because of the random spatial orientation of every tiny crystallite. h) Raman spectrum of the LG film. i) Absorption and photoluminescence spectra of the SG and LG films demonstrating a sharp cut-off and narrow ($\delta = 16.2$ nm) emission for the latter, respectively, owing to low concentration of shallow traps in large perovskite grains.

reason for such a narrowing stems from less concentration of shallow trap states scattering excitons as compared to that of the SG film. To prove this statement we measured PL spectra at temperature $T = 6$ K which throws light on the shallow trap-assisted radiative recombination mechanism (Figure S5, Supporting Information). For both films, the spectra show two emission peaks (Figure S5a, Supporting Information) associated with defect luminescence ($\lambda_{max} = 544$ nm) and recombination of defect-trapped excitons ($\lambda_{max} = 536$ nm). These localized excitons are spectrally well distinguished from free excitons ($\lambda_{max} = 529$ nm) observable in a defect-free perovskite nanowire crystal synthesized according to a protocol reported elsewhere.[15] Thus, all the results are in good agreement with those obtained for a Bridgman grown $CsPbBr_3$ single crystal.[28] After revealing the reason for the complex line shape of PL at $T = 6$ K we conducted pump fluence-dependent measurements. It turned out, in the LG film, excitonic emission grows up with fluence faster than in the SG film (Figure S5b–d, Supporting Information). For the former, such behavior is explained by shallow traps filling at lower fluence (i.e., lower concentration

of the traps) that gives rise to excitons undergoing rapid localization at defect sites.

2.2. Gain Measurements and Mechanisms Discussion

For the gain measurements, we used a fs mode-locked Ti:sapphire regenerative amplifier (Spectra Physics, Spitfire Pro) pulsed laser with a 120 fs pulse width and a 1 kHz repetition rate as optical pump source emitting at 800 nm which was frequency-doubled via BBO crystal to obtain an emission at 400 nm. For the ASE measurements, the pump power was adjusted using a neutral density filter and an optical beam having a stripe geometry was obtained focusing via a cylindrical lens. The signal from the sample film was collected with a fiber coupled to a spectrometer (Maya 2000 Pro) where the fiber is placed such that it shares the same longitudinal axis with the stripe-shaped beam exciting the sample film. To determine the laser beam size in our ASE measurements, we used a laser beam profiler with a low-resolution CCD camera offering built-in photodiode trigger (SP503U, Ophir-Spiricon), which measured intensity distribution, profile, and size of the beam, respectively. In the ASE experiments from the obtained films, we used two complementary approaches: spectral analysis at increasing fluences and fixed stripe length (**Figure 2**a–c), and PL intensity measurements at various fluences and stripe lengths (Figure 2d–f).

To perform VSL measurements, we placed an adjustable slit with only one sliding blade between the cylindrical lens and the sample film. To avoid common pitfalls of VSL measurement, we followed the listed protocol. First, to evade the effects of the interference, the distance between the slit and the sample is minimized. Second, in order to minimize the deviations caused by the change in the intensity of the beam throughout the excitation stripe, we created a relatively long (6 mm) stripe and used the center part of the beam. Finally, to interpret our data we implemented the small signal gain model, $I = \left(\frac{A}{g}\right)(e^{(g\times l)} - 1)$, where I is the PL intensity, A is the optical growth factor, g is the modal gain coefficient, and l is the stripe length of the excitation beam. This approach avoids any overestimation of gain coefficients.[29,30] In **Figure 3**a, the fluence range is from 30 up to almost 10 000 μJ cm^{-2}, which are the limits for ASE detection and structural damage of the films, respectively. Indeed, we observed some degradation of the perovskite film at fluences ≈5–10 mJ cm^{-2} (Figure S7, Supporting Information) depending on the film thickness and quality.

In perovskite $CsPbBr_3$ with exciton binding energy around 35 meV,[31] the excitons play a major role in the generation of optical gain. Usually, in halide perovskites, the gain dependence on incident pump fluence indicates a linear slope above the threshold and before saturation, where the material reaches the Mott density resulting in dissociation of excitons. The saturation at high carrier concentrations can be modeled by including a saturation term (N_s) in the equation of the material gain

$$g_m = \frac{\sigma(N - N_{th})}{1 + N/N_s} \quad (1)$$

where σ is the emission cross-section (or "dynamic gain" for semiconductors) of light-emitting material and N_{th} is the

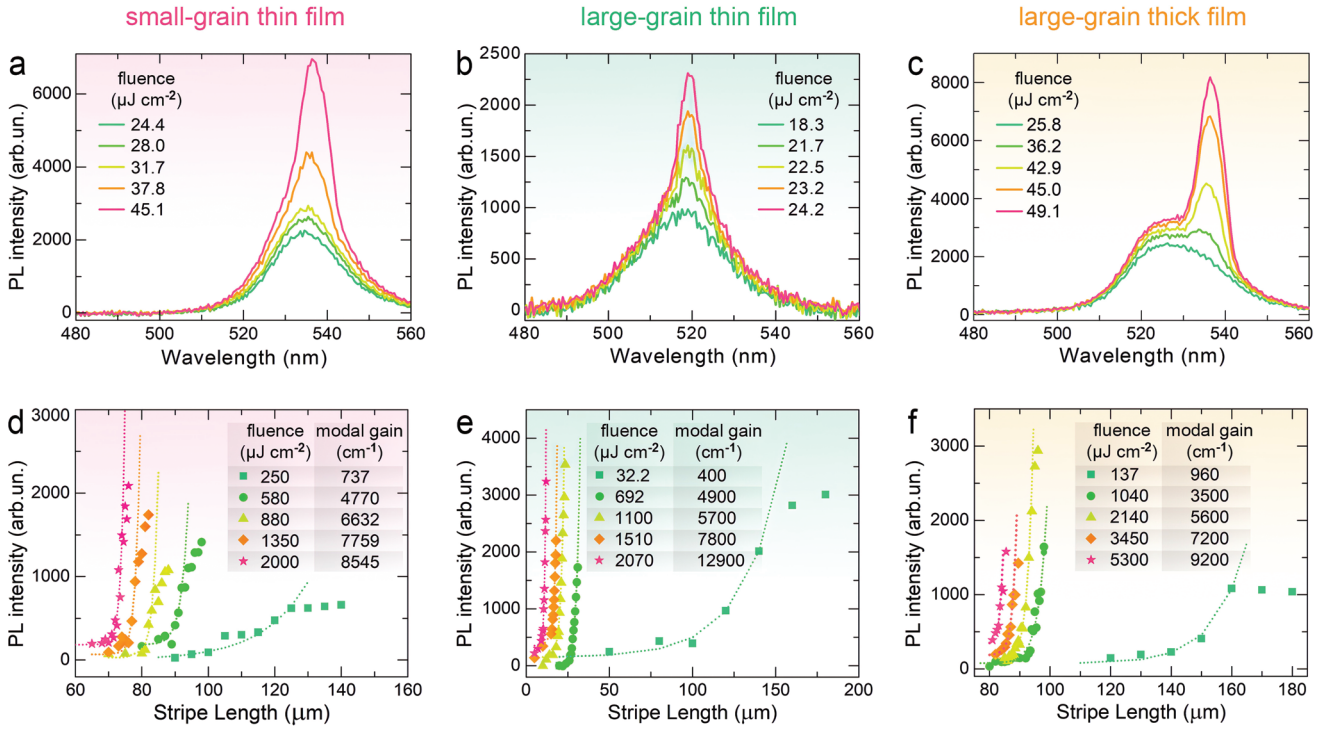

Figure 2. ASE measurements from $CsPbBr_3$ films. PL spectra at different fluences at fixed stripe length for a) small-grain film, b) large-grain thin (100 nm) film, c) large-grain thick (250 nm) film. PL dependence on stripe length at different fluences for d) small-grain film, e) large-grain thin (100 nm) film, f) large-grain thick (250 nm) film.

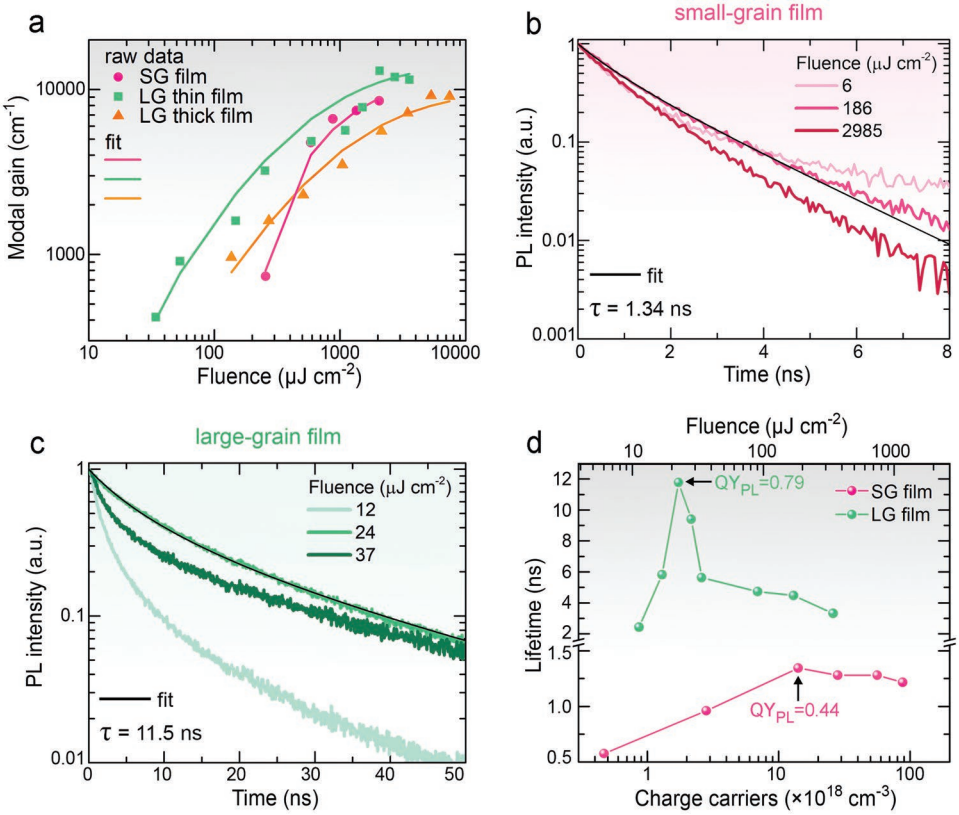

Figure 3. Fluence-dependent luminescent properties. a) Extracted modal gain dependence on laser fluence for small-grain, large-grain (100 nm) and large-grain (250 nm) films. b) Power-dependent time-resolved photoluminescence of small-grain $CsPbBr_3$ film. c) Power-dependent TRPL of large-grain $CsPbBr_3$ film. d) Power-dependent lifetime for small-grain and large-grain films extracted from TRPL spectra.

carrier density corresponding to the transparent condition (i.e., zero absorption). In the VSL experiments, the measured optical gain is modal (G) meaning that it takes into account at least the overlapping between the propagating mode structure and the pumped film (in assumption that gain is distributed homogeneously). To perform modal analyses, structures were modeled as planar waveguides consisting of a specific crystalline film with a certain amount of surface roughness between a quartz substrate (n = 1.45) and air (n = 1). The analyses for different wavelengths were performed using Lumerical FDE solver, a commercially available software. The mode profile determined the spatial distribution of fundamental transverse electric mode (TE0). The confinement factor Γ is the ratio of electric field intensity confined in the gain medium to the total electric field intensity. According to our calculations at λ = 540 nm, Γ ≈ 0.65 for the polycrystalline film, Γ ≈ 0.75 for the large-grain thin film, and Γ ≈ 0.96 for large-grain thick film (Figure S9, Supporting Information). As a result, the modal gain can be calculated as

$$G = \Delta \cdot g_m \quad (2)$$

On the basis of Equations (1) and (2), we fitted the experimental dependencies for modal gain shown in Figure 3a, where the fitting parameters are listed in **Table 1**. First of all, there is one order of magnitude difference between threshold carrier densities (N_{th}) needed for the achievement of transparency in small-grain (SG) films and large-grain (LG) films. This is in excellent agreement with our measurements of TRPL from these films, where we observed approximately ten times longer lifetimes for LG films (Figures 3b–d), meaning lower nonradiative losses for high-quality LG films.

Although the shallow defect states do not have a strong impact on room-temperature PL intensity because of charge trapping/detrapping processes, deep defect states always introduce significant nonradiative recombination.[34] Concentration of the latter can be estimated by analyzing PL decay (lifetime) at various pump fluence (Figures 3b–d and Figure S6, Supporting

Table 1. Parameters for fitting of the optical gain calculated with Equation 1 and Equation (2) for our $CsPbBr_3$ samples, as well as the values for bulk GaAs and GaN materials from literature[32,33] at room temperature.

Sample (thickness)	σ [10^{-16} cm^2]	N_{th} [10^{19} cm^{-3}]	N_s [10^{19} cm^{-3}]
$CsPbBr_3$ SG (70 nm)	4	1.5	5
$CsPbBr_3$ LG-thin (100 nm)	4	0.1	5
$CsPbBr_3$ LG-thick (250 nm)	1.5	0.1	7
GaAs (bulk)	1.3–1.5	0.12	–
GaN (bulk)	0.4	0.58	–

Table 2. Comparison of representative optical gain values reported for perovskite-based materials pumped by fs laser pulses at room temperature.

Material[a] (thickness)	Method	Threshold [μJ cm^{-2}]	Net gain [cm^{-1}]	PL max lifetime [ns]	Ref.
$CsPbBr_3$ NC film (1 μm)	Drop-casting	22	98 @ 57 μJ cm^{-2}	3.1	[42]
$CsPbBr_3$ film (200 nm)	Thermal evaporation	3.3	324 @ 44.1 μJ cm^{-2}	1.2	[43]
$CsPbBr_3$ NC film (<1 μm)	Spin-coating	5.3	450	5	[44]
$CsPbBr_3$ NC film (400 nm)	Drop-casting	12	580 @ 1500 μJ cm^{-2}	9	[45]
(CsFAMA)$PbBr_3$/NMA film (70 nm)	Spin-coating	1.44	1 176 @ 56.2 μJ cm^{-2}	2	[46]
$CsPbBr_3$ single-crystal film (300 nm)	Chemical vapor deposition	8	1 255 @ 160 μJ cm^{-2}	3.1	[35]
(CsFAMA)$PbBr_3$/NMA film (300 nm)	Spin-coating	3.8	3 030 @ 266 μJ cm^{-2}	2.3	[47]
$CsPbBr_3$ microcrystal (from hundred nm to few μm)	Chemical vapor deposition	14	5 077 @ 156 μJ cm^{-2}	–	[19]
$CsPbBr_3$ large-grain film (100 nm)	High-temperature recrystallization	14	12 900 @ 2070 μJ cm^{-2}	11.5	This work[b]

[a]NC: nanocrystals, FA: formamidinium, MA: methylammonium, NMA: naphthylmethylammonium; [b]Measured during 10^8 photoexcitation cycles at ambient conditions.

Information). As fluence increases, lifetime undergoes elongation, reaches the maximum value ($\tau = 1.34$ ns for SG film, and $\tau = 11.5$ ns for LG film), and then shortens. A similar behavior was reported by Zhong et al.[35] and Du et al.[19] for single-crystal $CsPbBr_3$ CVD film and microplates of the same composition, respectively. In terms of photoexcited charge carrier dynamics, the increase in lifetime with fluence occurs due to the filling of the deep trap states—source of nonradiative recombination. At a certain fluence, these states are completely filled, which results in the observation of almost monoexponential PL decay showing the largest lifetime value. For these decay curves, the quantum yield of PL (QY_{PL}) was evaluated using the "ABC model" proposed by Shen et al.[36] It was found that QY_{PL} for LG film is almost two times higher ($QY_{PL} \approx 79\%$) than for SG one ($QY_{PL} \approx 44\%$). Further increase in fluence invokes the acceleration of PL decay (lifetime shortening) because of radiative bimolecular recombination. The estimation of charge carrier density (for details, see Supporting Information) at the longest lifetimes (Figure 3d) makes it possible to determine concentrations of deep trap states 1.75×10^{18} and 14.2×10^{18} cm^{-3} in LG and SG films, respectively. In the case of the LG film, monoexponential PL decay has the longest lifetime among all the values reported for $CsPbBr_3$ microcrystals and films (**Table 2**). This implies high-temperature pressure-assisted recrystallization affords high-quality perovskite films with low concentrations of both shallow and deep defect states, which is critical for enabling low-threshold ASE or lasing.

In contrast, such parameters as stimulated emission cross-section (σ) and saturation carrier density (N_s) are similar for SG and LG films ($\approx 5\times 10^{19}$ cm^{-3}) with close thicknesses (70 and 100 nm, respectively). This is of the same order as the density for Mott transition $n_M = 1.19^2 k_B T/2a_b^3 E_b$ (for bulk $CsPbBr_3$ $n_M \approx 1 \times 10^{19}$ cm^{-3}[37]), where k_B is the Boltzmann constant, T is the temperature, a_B is the exciton Bohr radius, and E_b is the exciton binding energy. The thickness effect of the 250-nm thick LG film results in significant decrease of σ, because penetration length l_p (i.e., depth where intensity of the wave is decreased to $1/e^2$ of its incident value) at pump wavelength $\lambda = 400$ nm is around $l_p \approx 200$ nm, making the gain profile strongly inhomogeneous and reducing the averaged gain values.

The obtained coefficients also help to reveal the main difference between $CsPbBr_3$ with the other semiconductor materials. First of all, the determined values for σ up to 4×10^{-16} cm^2 are even up to two to three times higher than those observed previously for the best GaAs-based gain materials at room temperature: $\sigma = 1.5 \times 10^{-16}$ cm^2 with $N_{th} = 1.2 \times 10^{18}$ cm^{-3} (for GaAs) and $\sigma = 2.5 \times 10^{-16}$ cm^2 with $N_{th} = 1 \times 10^{18}$ cm^{-3} (for InGaAsP alloys[33,38]). Moreover, in our measurements, the best $CsPbBr_3$ LG-thin film possesses the maximum gain value well above 10 000 cm^{-1} (Figure 3a), which is a record value among the other lead bromide perovskites as shown in Table 2

To prove applicability of the high-gain large-grain $CsPbBr_3$ films, we carried out stability tests with 200-fs laser pulses at wavelength 515 nm and repetition rate 125 kHz at ambient conditions (25°C, and humidity 35%) without any encapsulation. The large-grain film demonstrated quite high stability with 20% decrease relatively the initial PL intensity after 4.5×10^8 photoexcitation cycles (for more details, see Figure S8a, Supporting Information and an additional description in Supporting Information), which is comparable to monocrystalline $CsPbBr_3$ nanostructures.[3,13] In addition, we conducted one more experiment on long-term photoluminescence stability of the non-encapsulated large-grain $CsPbBr_3$ thin film kept at ambient conditions by measuring its PL intensity every day for a week. As a result, no changes in a value for the intensity of PL peak were observed (Figure S8b, Supporting Information). To improve stability against humidity and oxygen in the atmosphere as well as to prevent toxic lead leakage, the perovskite layer can be further encapsulated into macroscale polymer matrices[39] and organic oxide glasses.[40] Indeed, encapsulation can solve several problems of lead halide perovskites such as their sensitivity to oxygen and moisture, and lead toxicity which is crucial for long-term environment-friendly applications.[41]

As a result, the high-quality $CsPbBr_3$ large-grain perovskite films fabricated by relatively simple and cost-effective approaches can exhibit high gain values similar to epitaxially grown III–V bulk semiconductors at room temperature, which are already standard for plenty of technological processes in optoelectronics.[38] This fact makes such films prospective for the creation of micro- and nano-lasers by various lithography techniques, which is discussed in the next section.

2.3. Fabrication and Characterization of Perovskite Microlasers

To fabricate the microdisc perovskite lasers we employed a direct fs-laser multi-pulse imprinting on the 100-nm thick perovskite film on a silica glass substrate with a specially designed laser beam having a donut-shaped lateral intensity profile, as schematically shown in **Figure 4**a. The proposed technology is convenient for rapid and high throughput fabrication of microlaser arrays as well as more complicated designs. Moreover, the technology is promising for up-scaling and application in optoelectronic devices, allowing to produce areas of cm^2 in scale with closely packed perovskite lasers.[22] This approach has an advantage over such time-consuming and costly techniques as focused-ion-beam milling,[48] whereas the fabrication design is more flexible as compared to the nanoimprinting technique.[49]

To realize the optimized laser patterning conditions, we used laser projection lithography with flat-top beam in form of ring shown in Figure 4a. The perovskite microdisc lasers were fabricated using direct ablation with 515-nm (second-harmonics) and 220-fs laser pulses generated by a Yb:KGW-based laser system (Pharos, Light Conversion). The output Gaussian-shape pulses were first shaped into the donut-shaped beam using a specially designed amplitude mask. The mask was arranged within a 4-f optical scheme for projection of the beam into a focused spot with similar intensity distribution. The shaped pulses were then focused with a dry microscope objective (15×, NA =0.32) yielding a 10-µm wide focal-plane diameter of the donut-shaped pattern. The perovskite film were arranged onto a PC-driven nanopositioning system (Newport XM series) providing the movement accuracy better than 100 nm along all three axes. The schematic of the experimental setup used for laser printing is given elsewhere.[23] All details of the experimental setup used for laser projection lithography can be found elsewhere.[25] SEM image of a microdisc fabricated in a single-shot regime at fluence $F \approx 100$ mJ cm^{-2} clearly demonstrates the advantages of the applied laser printing approach, providing the delicate gradual material removal from the donut-shaped area without any visible damage of the remaining isolated microdisc (Figure 4b). At these optimal laser irradiation conditions, the sidewalls of the perovskite microdisc are free of melting as the laser-induced removal proceeds within a narrow ring-shaped volume of the high-quality perovskite film.

Lasing properties of single microdisc were studied under optical excitation at a wavelength of 515 nm using 220-fs laser pulses of a regenerative amplified Yb:KGW-based laser system. The laser beam was focused onto the sample surface at normal incidence by a microscope objective (5×, NA = 0.14) aligned to provide uniform irradiation of the microdiscs (Gaussian distribution with an FWHM of ≈20 µm). The laser emission of a single microdisc was collected in transmission configuration using an infinity corrected microscope objective (100×, NA = 0.95) and analyzed with a spectrometer (Andor Shamrock 303i) equipped with a cooled electron multiplying CCD camera (Andor Newton 970). The residual light from the excitation beam was blocked by a 550 nm long-pass filter (FELH0550). The emission of single microdisc above the lasing threshold was spatially and spectrally resolved using a 1200 grooves per mm grating and a slit width of 10 µm at the entrance of the spectrometer. All measurements were performed at normal conditions and reproduced several times.

Figure 4c shows the spectral evolution of PL with the increase of the laser pump fluence for a microdisc with diameter 10 µm. The observed behavior demonstrates all basic lasing features: clear threshold for emission at a lasing mode at around $F \approx 14$–16 µJ cm^{-2} and its sharp spectral narrowing by two orders of magnitude (from 38 nm down to 0.3 nm) at the red-wing ($\lambda = 530$–540 nm) of excitonic PL spectra as shown in Figure 4d. Such low thresholds are very close to the threshold of ASE in such films, where optical gain appears. The observed

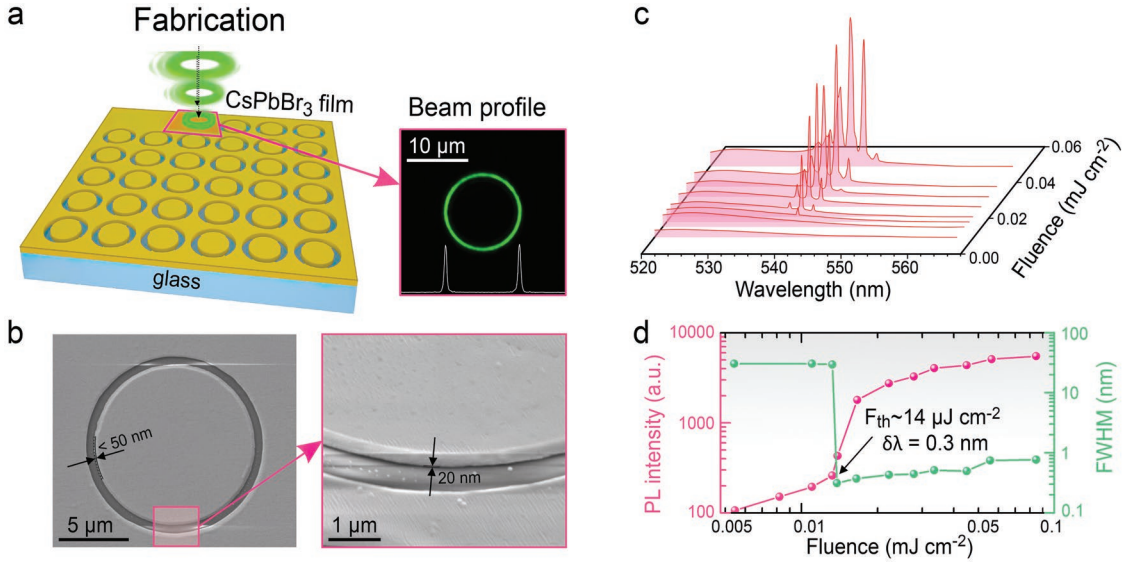

Figure 4. Lasing properties of a single microdisc. a) Schematic illustration of fabrication of perovskite microlasers and a photograph of the donut-shaped laser beam. b) SEM image of perovskite microdisc laser. Arrows indicate high smoothness of the microdisc wall (roughness is less than 50 nm and gap with substrate is less 20 nm). c) Photoluminescence spectra for $D = 10$ µm microdisc of $CsPbBr_3$ at different intensities below and after the lasing threshold. d) Intensity and full-width-half-maximum (FWHM) of emission spectrum of the microdisc at the lasing wavelength.

multimode regime confirms the high quality of the microdisc, because high roughness would reduce mode number and increase lasing threshold.[22] Some discrepancy between threshold fluences for lasing and ASE in literature (see Table 2) might be originated from the various definitions of spot-size and fluence, whereas modal gain is a more universal parameter which can be compared directly.

3. Conclusion

We have demonstrated experimentally that high-quality $CsPbBr_3$ film with optimized thickness ≈100 nm exhibits the modal gain values exceeding 10 000 cm^{-1} level, which is the highest value among bulk halide perovskite materials. Moreover, at room temperature conditions, the achieved modal gain coefficients are comparable to the best gain systems of bulk GaN[50] and GaAs, and also on par with the best epitaxial quantum dot systems (e.g., InAs/GaAs[51]) or colloidal nanocrystals.[52] Such high values of gain explain why $CsPbBr_3$ material allowed for creation of a record-small non-plasmonic nanolaser for visible range at room temperature.[13] Remarkably, the studied large-grain $CsPbBr_3$ films fabricated by high-temperature pressure-assisted recrystallization method exhibit high photostability at ambient conditions without encapsulation.

The developed material platform is promising for low-intensity polaritonics, where large-scale high-quality films are highly demanded,[53] because threshold value for the carrier densities (≈10^{18} cm^{-3}) in LG thin films are well below the Mott transition ($n_M \approx 1 \times 10^{19}$ cm^{-3}). On the other hand, lower-quality SG films support photonic lasing only, because the threshold carrier density is comparable with the characteristic Mott density.

As an outlook, we envision that lasers with high and switchable gain (see works on single-crystal perovskites[19,54]) will be a promising direction, where large scale high-quality perovskite thin films would allow for creation of advanced photonic designs with various nanopatterning approaches. Also, the high-quality films will be beneficial for integration with other emerging functional materials for novel devices.[55,56]

4. Experimental Section

Materials: Cesium bromide (CsBr, TCI Chemicals), lead(II) bromide ($PbBr_2$, 99.998% trace metals basis, TCI Chemicals), dimethyl sulfoxide anhydrous (DMSO, anhydrous ≥99.8%, Sigma-Aldrich) were used as received.

Preparation of Perovskite Precursor Solutions: $PbBr_2$ (62 mg, 0.3 mmol) and CsBr (110 mg, 0.3 mmol) were mixed and dissolved in DMSO (1100 mg, 1 mL) by shaking for 5 min to obtain a clear 0.3 M solution. The solution was stored in a N_2-filled glove box to avoid exposure to oxygen and moisture. The solution was filtered through a 0.45 µm PTFE syringe adapter right before the perovskite film deposition.

$CsPbBr_3$ Source Films Preparation: The glass substrates (15 × 15 mm^2) were subsequently cleaned with Na_2CO_3 powder, ultrasonicated in deionizied water and 2-propanol for 5 min, and, finally, exposed to O_3 for 10 min. To produce thin (100 nm) and thick (250 nm) large-grain films thin (70–80 nm) and thick (100–110 nm) small-grain films were employed, respectively. Small-grain films were prepared using the same perovskite precursor solution spin-casted at 3000 rpm or 1500 rpm for 5 min. Thereafter, the samples were gradually annealed on a hot plate from 50 to 130 °C at 5 °C min^{-1} rate. The films deposition and annealing was carried out in a N_2-filled glove box with both moisture and oxygen concentration not exceeding 2 ppm.

Fabrication of Large-Grain $CsPbBr_3$ Films: High-temperature pressure-assisted recrystallization of two source samples pressed down in a face-to-face manner was performed using a PZ 28-3TD titanium plate (Harry Gestigkeit) equipped with PR 5-3T programmer. The following mode was chosen for the annealing: the temperature increases from 30 °C up to 510 °C for 15 min, and then slowly goes down to room temperature for 3 h.

Structure Characterization: SEM images were obtained on scanning electron microscope FEI Quanta Inspect. High-resolution TEM images were obtained on a Zeiss Libra 200FE transmission electron microscope equipped with field emission cathode, OMEGA energy filter, and Köhler illumination system. AFM images of surface morphology of perovskite thin films were measured on an atomic field microscope AIST Smart SPM. XRD pattern of the large-grain film was recorded in the Θ–Θ geometry on XRD-7000 diffractometer (Shimadzu) equipped with a 2 kW rotating Cu anode tube. The measurements were carried out in the scan range 2Θ from 10° to 60° with 0.002° precision. Raman spectra of the large-grain film were obtained on a confocal Raman microscope inVia Renishaw.

Lifetime Measurements: The lifetime measurements were carried out on a three-channel optical microscope of own design. A fs laser Pharos (Light Conversion) was used as a pump source, the connection of which is used to generate radiation with a wavelength of 405 nm in optical parametric amplifier (OPA) Orpheus-HP (Light Conversion). The radiation frequency was 100 kHz, the pulse duration about 150 fs. Pump radiation with a wavelength of 405 nm illuminated the sample from above; the lifetime signal was also collected from above through a M plan Apo 50× objective (Mitutoyo) with NA = 0.55. To match the pump arm and the collection channel a DMSP490 dichroic mirror (Thorlabs) with a cutoff wavelength of 490 nm was employed. A photoluminescence signal was recorded with MPD-PD-100-CTC-FC single-photon radiation detector which was connected to a TCSPC PicoHarp 300 unit (PicoQuant). The pump power was controlled by PD300-TP power meter (Ophir).

Supporting Information

Supporting Information is available from the Wiley Online Library or from the author.

Acknowledgements

This work was supported by Priority 2030 Federal Academic Leadership Program and the Ministry of Science and Higher Education of the Russian Federation (Project 075-15-2021-589). The work was partially done in ITMO Core Facility Center "Nanotechnologies." XRD measurements were performed in North Ossetian State University Core Shared Research Facility (NOSU CSRF) "Physics and Technology of Nanostructures" and were supported by the Ministry of Science and Higher Education of the Russian Federation (project 075-15-2021-1349). TEM study was carried out by the Interdisciplinary Resource Centre for Nanotechnology of SPbSU. The authors thank Mr. Ivan Pustovit for assistance in graphic design.

Conflict of Interest

The authors declare no conflict of interest.

Data Availability Statement

The data that support the findings of this study are available from the corresponding author upon reasonable request.

Keywords

halide perovskites, laser ablation, microlasers, optical gain

Received: October 18, 2022
Revised: December 18, 2022
Published online: January 29, 2023

[1] H. Zhu, Y. Fu, F. Meng, X. Wu, Z. Gong, Q. Ding, M. V. Gustafsson, M. T. Trinh, S. Jin, X. Zhu, *Nat. Mater.* **2015**, *14*, 636.
[2] Y. Fu, H. Zhu, A. W. Schrader, D. Liang, Q. Ding, P. Joshi, L. Hwang, X. Zhu, S. Jin, *Nano Lett.* **2016**, *16*, 1000.
[3] S. W. Eaton, M. Lai, N. A. Gibson, A. B. Wong, L. Dou, J. Ma, L.-W. Wang, S. R. Leone, P. Yang, *Proc. Natl. Acad. Sci. U. S. A.* **2016**, *113*, 1993.
[4] K. Park, J. W. Lee, J. D. Kim, N. S. Han, D. M. Jang, S. Jeong, J. Park, J. K. Song, *J. Phys. Chem. Lett.* **2016**, *7*, 3703.
[5] C. Li, Z. Liu, Q. Shang, Q. Zhang, *Adv. Opt. Mater.* **2019**, *7*, 1900279.
[6] D. I. Markina, A. P. Pushkarev, I. I. Shishkin, F. E. Komissarenko, A. S. Berestennikov, A. S. Pavluchenko, I. P. Smirnova, L. K. Markov, M. Vengris, A. A. Zakhidov, S. V. Makarov, *Nanophotonics* **2020**, *9*, 3977.
[7] K. R. Safronov, A. A. Popkova, D. I. Markina, A. P. Pushkarev, S. V. Makarov, V. O. Bessonov, A. A. Fedyanin, *Laser Photonics Rev.* **2022**, *16*, 2100728.
[8] Y. J. Li, Y. Lv, C.-L. Zou, W. Zhang, J. Yao, Y. S. Zhao, *J. Am. Chem. Soc.* **2016**, *138*, 2122.
[9] P. Cegielski, A. L. Giesecke, S. Neutzner, C. Porschatis, M. Gandini, D. Schall, C. Perini, J. Bolten, S. Suckow, S. Kataria, B. Chmielak, T. Wahlbrink, A. Petrozza, M. Lemme, *Nano Lett.* **2018**, *18*, 6915.
[10] P. Trofimov, A. P. Pushkarev, I. S. Sinev, V. V. Fedorov, S. Bruyere, A. Bolshakov, I. S. Mukhin, S. V. Makarov, *ACS Nano* **2020**, *14*, 8126.
[11] A. S. Polushkin, E. Y. Tiguntseva, A. P. Pushkarev, S. V. Makarov, *Nanophotonics* **2020**, *9*, 599.
[12] Z. Liu, J. Yang, J. Du, Z. Hu, T. Shi, Z. Zhang, Y. Liu, X. Tang, Y. Leng, R. Li, *ACS Nano* **2018**, *12*, 5923.
[13] E. Tiguntseva, K. Koshelev, A. Furasova, P. Tonkaev, V. Mikhailovskii, E. V. Ushakova, D. G. Baranov, T. Shegai, A. A. Zakhidov, Y. Kivshar, S. V. Makarov, *ACS Nano* **2020**, *14*, 8149.
[14] J. Xing, X. F. Liu, Q. Zhang, S. T. Ha, Y. W. Yuan, C. Shen, T. C. Sum, Q. Xiong, *Nano Lett.* **2015**, *15*, 4571.
[15] A. P. Pushkarev, V. I. Korolev, D. I. Markina, F. E. Komissarenko, A. Naujokaitis, A. Drabavicius, V. Pakstas, M. Franckevicius, S. A. Khubezhov, D. A. Sannikov, A. V. Zasedatelev, P. G. Lagoudakis, A. A. Zakhidov, S. V. Makarov, *ACS Appl. Mater. Interfaces* **2019**, *11*, 1040.
[16] Q. Zhang, S. T. Ha, X. Liu, T. C. Sum, Q. Xiong, *Nano Lett.* **2014**, *14*, 5995.
[17] Q. Zhang, R. Su, X. Liu, J. Xing, T. C. Sum, Q. Xiong, *Adv. Funct. Mater.* **2016**, *26*, 6238.
[18] R. Su, C. Diederichs, J. Wang, T. C. Liew, J. Zhao, S. Liu, W. Xu, Z. Chen, Q. Xiong, *Nano Lett.* **2017**, *17*, 3982.
[19] W. Du, X. Wu, S. Zhang, X. Sui, C. Jiang, Z. Zhu, Q. Shang, J. Shi, S. Yue, Q. Zhang, X. Liu, *Nano Lett.* **2022**, *22*, 4049.
[20] N. Zhang, W. Sun, S. P. Rodrigues, K. Wang, Z. Gu, S. Wang, W. Cai, S. Xiao, Q. Song, *Adv. Mater.* **2017**, *29*, 1606205.
[21] X. Yang, J. Wu, T. Liu, R. Zhu, *Small Methods* **2018**, *2*, 1800110.
[22] A. Zhizhchenko, S. Syubaev, A. Berestennikov, A. V. Yulin, A. Porfirev, A. Pushkarev, I. Shishkin, K. Golokhvast, A. A. Bogdanov, A. A. Zakhidov, A. A. Kuchmizhak, Y. S. Kivshar, S. V. Makarov, *ACS Nano* **2019**, *13*, 4140.
[23] A. Y. Zhizhchenko, P. Tonkaev, D. Gets, A. Larin, D. Zuev, S. Starikov, E. V. Pustovalov, A. M. Zakharenko, S. A. Kulinich, S. Juodkazis, A. A. Kuchmizhak, S. V. Makarov, *Small* **2020**, *16*, 2000410.
[24] A. Zhizhchenko, A. Cherepakhin, M. Masharin, A. Pushkarev, S. Kulinich, A. Porfirev, A. Kuchmizhak, S. Makarov, *Laser Photonics Rev.* **2021**, *15*, 2100094.
[25] A. Y. Zhizhchenko, A. B. Cherepakhin, M. A. Masharin, A. P. Pushkarev, S. A. Kulinich, A. A. Kuchmizhak, S. V. Makarov, *Nano Lett.* **2021**, *21*, 10019.
[26] D. Dores, L. Souza, J. Giehl, V. Ludwig, V. Silva, V. Oliveira, R. Costa, T. Pacheco, C. Rodrigues, C. Pinotti, Z. M. Costa, *Blucher Proc.* **2019**, *6*, 1.
[27] M. Rodová, J. Brožek, K. Knížek, K. Nitsch, *J. Therm. Anal. Calorim.* **2003**, *71*, 667.
[28] J. Peters, Z. Liu, O. Bulgin, Y. He, V. Klepov, M. De Siena, M. Kanatzidis, B. Wessels, *J. Phys. Chem. Lett.* **2021**, *12*, 9301.
[29] K. Shaklee, R. Leheny, *Appl. Phys. Lett.* **1971**, *18*, 475.
[30] A. L. Alvarado-Leaños, D. Cortecchia, G. Folpini, A. R. Srimath Kandada, A. Petrozza, *Adv. Opt. Mater.* **2021**, *9*, 2001773.
[31] T. G. Liashenko, E. D. Cherotchenko, A. P. Pushkarev, V. Pakštas, A. Naujokaitis, S. A. Khubezhov, R. G. Polozkov, K. B. Agapev, A. A. Zakhidov, I. A. Shelykh, S. V. Makarov, *Phys. Chem. Chem. Phys.* **2019**, *21*, 18930.
[32] W. Fang, S. Chuang, *Appl. Phys. Lett.* **1995**, *67*, 751.
[33] O. Svelto, D. C. Hanna, *Principles of Lasers*, Vol. *4*, Springer, Berlin, Heidelberg **1998**.
[34] H. Jin, E. Debroye, M. Keshavarz, I. G. Scheblykin, M. B. Roeffaers, J. Hofkens, J. A. Steele, *Mater. Horiz.* **2020**, *7*, 397.
[35] Y. Zhong, K. Liao, W. Du, J. Zhu, Q. Shang, F. Zhou, X. Wu, X. Sui, J. Shi, S. Yue, Q. Wang, Y. Zhang, Q. Zhang, X. Hu, X. Liu, *ACS Nano* **2020**, *14*, 15605.
[36] Y. Shen, G. Mueller, S. Watanabe, N. Gardner, A. Munkholm, M. Krames, *Appl. Phys. Lett.* **2007**, *91*, 141101.
[37] R. Su, A. Fieramosca, Q. Zhang, H. S. Nguyen, E. Deleporte, Z. Chen, D. Sanvitto, T. C. Liew, Q. Xiong, *Nat. Mater.* **2021**, *20*, 1315.
[38] E. Rosencher, B. Vinter, *Optoelectronics*, Cambridge University Press, Cambridge **2002**.
[39] S. N. Raja, Y. Bekenstein, M. A. Koc, S. Fischer, D. Zhang, L. Lin, R. O. Ritchie, P. Yang, A. P. Alivisatos, *ACS Appl. Mater. & interfaces* **2016**, *8*, 35523.
[40] I. Konidakis, A. Karagiannaki, E. Stratakis, *Nanoscale* **2022**, *8*, 2966.
[41] P. Docampo, T. Bein, *Acc. Chem. Res.* **2016**, *49*, 339.
[42] Y. Wang, X. Li, J. Song, L. Xiao, H. Zeng, H. Sun, *Adv. Mater.* **2015**, *27*, 7101.
[43] L. Zhang, F. Yuan, H. Dong, B. Jiao, W. Zhang, X. Hou, S. Wang, Q. Gong, Z. Wu, *ACS Appl. Mater. Interfaces* **2018**, *10*, 40661.
[44] S. Yakunin, L. Protesescu, F. Krieg, M. I. Bodnarchuk, G. Nedelcu, M. Humer, G. De Luca, M. Fiebig, W. Heiss, M. V. Kovalenko, *Nat. Commun.* **2015**, *6*, 8056.
[45] Y. Xu, Q. Chen, C. Zhang, R. Wang, H. Wu, X. Zhang, G. Xing, W. W. Yu, X. Wang, Y. Zhang, M. Xiao, *J. Am. Chem. Soc.* **2016**, *138*, 3761.
[46] Y. Liang, Q. Shang, M. Li, S. Zhang, X. Liu, Q. Zhang, *Adv. Funct. Mater.* **2021**, *31*, 2106108.
[47] M. Li, Q. Shang, C. Li, S. Li, Y. Liang, W. Yu, C. Wu, L. Zhao, Y. Zhong, W. Du, X. Wu, Z. Jia, Y. Gao, H. Chen, X. Liu, S. Guo, Q. Liao, G. Xing, L. Xiao, Q. Zhang, *Adv. Funct. Mater.* **2021**, *31*, 2102210.
[48] M. S. Alias, I. Dursun, D. Shi, M. I. Saidaminov, E. M. Diallo, D. Priante, T. K. Ng, O. M. Bakr, B. S. Ooi, *J. Vac. Sci. Technol., B: Microelectron. Nanometer Struct.–Process., Meas., Phenom.* **2015**, *33*, 051207.

[49] N. Pourdavoud, S. Wang, A. Mayer, T. Hu, Y. Chen, A. Marianovich, W. Kowalsky, R. Heiderhoff, H.-C. Scheer, T. Riedl, *Adv. Mater.* **2017**, *29*, 1605003.
[50] R. Dingle, K. Shaklee, R. Leheny, R. Zetterstrom, *Appl. Phys. Lett.* **1971**, *19*, 5.
[51] C. Lingk, G. von Plessen, J. Feldmann, K. Stock, M. Arzberger, G. Böhm, M.-C. Amann, G. Abstreiter, *Appl. Phys. Lett.* **2000**, *76*, 3507.
[52] B. Guzelturk, M. Pelton, M. Olutas, H. V. Demir, *Nano Lett.* **2018**, *19*, 277.
[53] R. Tao, K. Peng, L. Haeberlé, Q. Li, D. Jin, G. R. Fleming, S. Kéna-Cohen, X. Zhang, W. Bao, *Nat. Mater.* **2022**, *21*, 761.
[54] J. Tian, G. Weng, Y. Liu, S. Chen, F. Cao, C. Zhao, X. Hu, X. Luo, J. Chu, H. Akiyama, S. Chen, *Commun. Phys.* **2022**, *5*, 160.
[55] P. Tonkaev, I. S. Sinev, M. V. Rybin, S. V. Makarov, Y. Kivshar, *Chem. Rev.* **2022**, *122*, 15414.
[56] A. Elbanna, K. Chaykun, Y. Lekina, Y. Liu, B. Febriansyah, S. Li, J. Pan, Z. X. Shen, J. Teng, *Opto-Electron. Sci.* **2022**, *1*, 220006.